

# Ultralow-loss diamond nanomechanics enabled by van der Waals self-assembly

Guanhao Huang,<sup>1,\*</sup> Chang Jin,<sup>1</sup> Sophie Weiyi Ding,<sup>1</sup> and Marko Lončar<sup>1,†</sup>

<sup>1</sup>*John A. Paulson School of Engineering and Applied Sciences, Harvard University, Cambridge, MA 02138, USA*

Nanomechanical systems are critical platforms for precision measurement, sensing, macroscopic quantum physics, and emerging quantum-information technologies. In these applications, high mechanical quality factors, often achieved using dissipation dilution, are important since they directly enhance measurement sensitivity and quantum coherence. However, surface stiction intrinsic to nanoscale structures severely limits their performance. Here, we transform this longstanding obstacle into a solution for tension-enabled dissipation dilution, via a novel van der Waals (vdW) self-assembly method. Leveraging intrinsic nanoscale surface interactions, we achieve controlled tensile stresses up to 1.3 GPa in single-crystal diamond—an ideal but notoriously difficult material to strain-engineer—without introducing additional interface losses. We demonstrate mechanical quality factors exceeding 100 million at 5 K, surpassing state-of-the-art systems at comparable aspect ratios. This versatile approach, applicable to other crystalline materials, opens up avenues using cryogenic nanomechanical systems for ultra-precise quantum sensing, tests of quantum gravity, and hybrid quantum systems.

Achieving ultralow-loss mechanical system is central to quantum science and precision measurement, as dissipation inherently limits sensitivity by introducing fluctuations into measurement systems according to the fluctuation-dissipation theorem [1]. A prominent example is application of crystalline mirror coatings [2, 3] in gravitational-wave detectors such as LIGO, where reducing thermal-mechanical noise significantly enhances detection precision. Nanomechanical oscillators have recently emerged as promising platforms for exploring macroscopic quantum phenomena due to their small mass [4], facilitating rapid quantum control and efficient transduction across diverse physical domains. Despite these advantages, a substantial gap persists between the mechanical quality factors achievable in bulk solids and their nanoscale counterparts, largely due to losses governed by a surface-to-volume scaling relationship [5]. This inherent trade-off between quantum-coherent coupling and acoustic losses presents a major obstacle for high-precision quantum nanomechanical applications.

Over the past decade, however, strained nanomechanical resonators have significantly advanced, surpassing previous benchmarks set by bulk crystalline resonators at both ambient and cryogenic temperatures. This breakthrough is enabled by dissipation dilution [6], a technique that substantially reduces mechanical losses by combining static tensile strain and geometric nonlinearity. State-of-the-art resonators typically utilize thin-film platforms featuring intrinsic tensile stresses around 1 GPa, generated by either thermal-expansion [7] or epitaxial lattice mismatch [8]. When paired with high aspect ratio designs, the acoustic quality factor is greatly enhanced according to  $Q = D_Q Q_{\text{int}}$ , with dilution factor [6]:

$$D_Q = 1 + \frac{1}{\alpha\lambda + \beta\lambda^2}, \quad \lambda = \sqrt{\frac{\epsilon}{12}} r,$$

where  $r = h/L$  represents device aspect ratio,  $\epsilon$  the tensile strain.  $\alpha$  and  $\beta$  are geometry-dependent form factors, which characterize clamping and distributed losses respectively. Since dissipation dilution is fundamentally material-agnostic [9], substantial efforts have shifted from the widely accessible amorphous silicon nitride (SiN) towards the more challenging crystalline materials, known for inherently lower acoustic damping at cryogenic conditions. While significant research effort have targeted strained crystalline materials such as SiC [10–12], InGaP [13], Si [8], and AlN [14], none have so far surpassed the SiN performance [15] (see Fig. 1(a) and Table I), except for cryogenic strained silicon (sSi), primarily due to the difficulty in achieving high crystal quality under epitaxial strain. Even strained silicon offers only modest improvement, with intrinsic losses approximately twice as low.

Thus, despite extensive research, the immense potential of cryogenic crystalline resonators remains largely unrealized. Among the candidates, single-crystal diamond uniquely stands out due to its low defect density, unmatched acoustic velocity, extraordinary thermal conductivity, wide optical transparency window, and inherent suitability for quantum applications owing to the naturally hosted color centers [16]. These superior properties position diamond as an ideal material for ultra-coherent nanomechanical devices. However, achieving high-quality factors in diamond has remained challenging. While promising mechanical quality factors of approximately  $10^6$  have been demonstrated in monolithic diamond cantilevers [17], the absence of intrinsic tensile stress in bulk diamond has precluded effective dissipation dilution. Straining bulk diamond through external mechanical forces is in principle possible, achieving 1 GPa of tensile stress would require forces of several thousand newtons on a standard diamond chip. In practice, however, bulk diamond is extremely brittle and typically fractures under tensile stresses exceeding 200 MPa [18]. In contrast, nanoscale experiments indicate its elastic tensile stress can surpass 35 GPa [19, 20], approaching the

\* [guanhao\\_huang@seas.harvard.edu](mailto:guanhao_huang@seas.harvard.edu)

† [loncar@seas.harvard.edu](mailto:loncar@seas.harvard.edu)

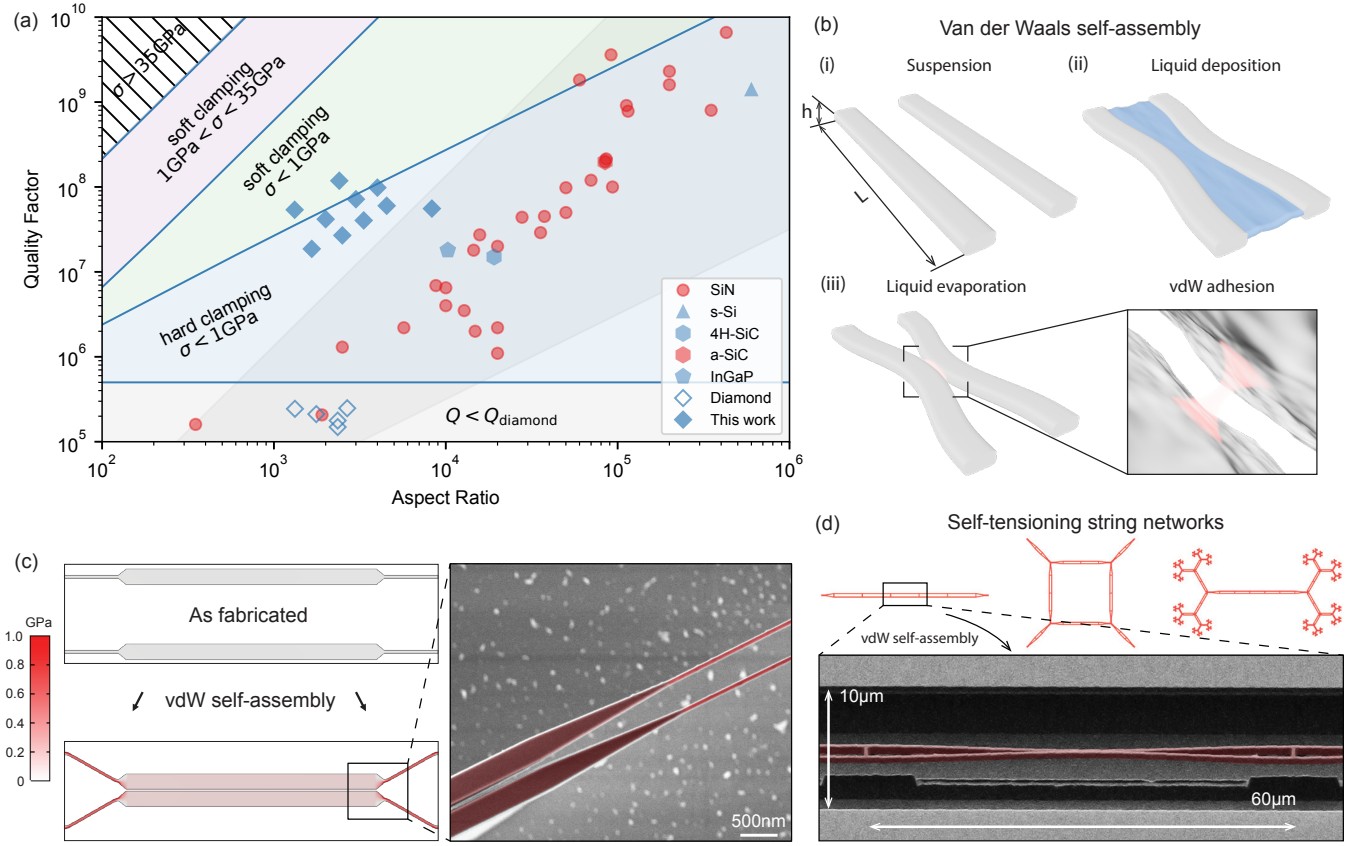


**FIG. 1. Ultralow-loss diamond nanomechanics using van der Waals (vdW) self-assembly.** (a) Acoustic quality factor as a function of aspect ratio ( $r = L/h$ ) for various nanomechanical materials ( $<200 \text{ nm}$  thick) down to liquid-helium temperature. Amorphous (red) and crystalline (blue) platforms are shown, including silicon nitride (SiN), strained silicon (s-Si), 4H-SiC, amorphous SiC (a-SiC), InGaP, non-tensioned diamond. The van der Waals (vdW) self-assembled diamond devices demonstrated in this work achieve quality factors exceeding  $10^8$ , significantly surpassing state-of-the-art devices at comparable aspect ratios. Shaded regions indicate typical scaling behaviors from  $\propto r$  (hard clamping) to  $\propto r^2$  (soft clamping). Theoretical projections for optical-grade diamond (100-nm thickness) under varying tensile stress highlight unprecedented performance achievable due to its exceptional intrinsic quality factor  $Q_{\text{int}} = 5 \times 10^5$  (horizontal blue line). (b) Schematic of the vdW self-assembly process: initially (i) suspended, non-tensioned diamond nanobeams fabricated via quasi-isotropic etching are drawn together by (ii) pico-liter water condensation. Upon evaporation, (iii) liquid tension facilitates stable adhesion through vdW surface interactions. (c) Finite element (FEM) schematic (not to scale) and false-color scanning electron microscopy (SEM) images of the vdW self-assembled double-beam resonator. Significant tensile stresses ( $1 \text{ GPa}$ ) develop within the narrow beam regions upon adhesion of the central areas. (d) False-color SEM image of segmented self-tensioning tethers enabling vdW self-assembly of complex string networks capable of supporting soft-clamped modes (vertical and horizontal axes scaled differently; viewing angle: 45 degrees).

10% theoretical strain limit. At the nanoscale, however, the lack of available large-scale, high-quality diamond thin films [21] has significantly impeded the practical realization of low-loss, high-aspect-ratio devices. Previous attempts to induce strain in monolithic diamond structures using electrostatic methods [22] have reached bending stresses around 200 MPa, but these methods have been limited by additional resistive losses arising from electromechanical coupling, severely compromising the mechanical coherence.

In this work, we overcome this longstanding challenge of engineering significant tensile strain in monolithic crystalline oscillators. As a result, we achieve strong dissipation dilution in ultralow-loss diamond nanomechanical

oscillators at cryogenic temperatures. Our devices consist of monolithic, high-aspect-ratio, string-like nanomechanical devices on single-crystal diamond, that self-assemble (procedure see Fig. 1(b)) to generate tensile strain through structural deformation. In our platform, we first demonstrate record-high surface-loss-limited intrinsic mechanical quality factors at liquid-helium temperature in diamond nanomechanics of various grades (see Table I). Building on this result, we introduce an effective strain-engineering method using van der Waals (vdW) self-assembly to impart tensile stresses up to 1.3 GPa (see Fig. 1(c)). Traditionally perceived as a significant challenge in suspending high-aspect-ratio structures, the carefully controlled vdW nanoscale interac-

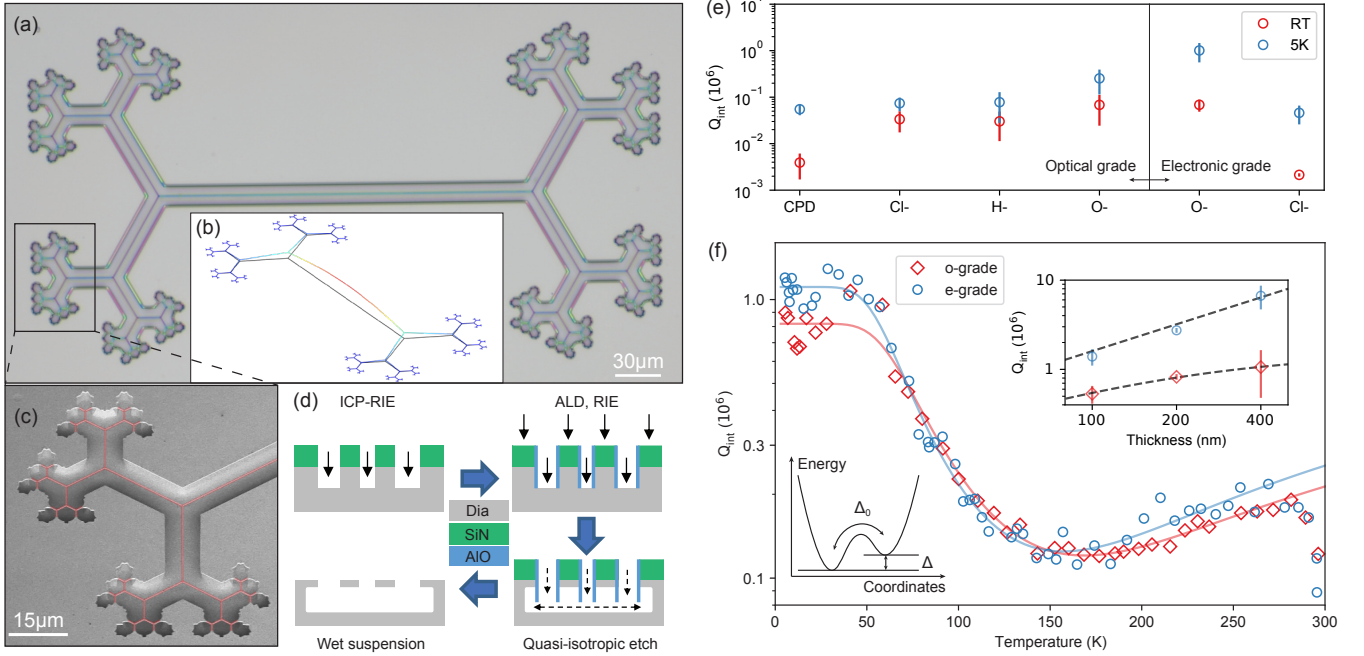


**FIG. 2. Optimal material loss study using soft-clamped diamond nanomechanics.** (a) Optical image of a suspended hierarchical diamond string oscillator with up to six branchings, accompanied by (c) a false-color SEM image detailing the suspended nanomechanical strings within isotropically etched diamond trenches. (b) Finite element modeling (FEM) of the fundamental vibrational mode illustrating a soft-clamped displacement profile under zero tension, reducing radiation losses caused by clamp overhang by more than 100-fold. (d) Simplified fabrication flow starts with etching nanoscale features in bulk diamond crystal using SiN hardmask. Next, atomic layer deposition (ALD) is used for sidewall protection, followed by quasi-isotropic oxygen plasma etching to undercut the structures, enabling the suspension of high-aspect-ratio slab-like nanomechanical string devices from single-crystal diamond plates. (e) Comparison of intrinsic quality factor  $Q_{\text{int}}$  for 100-nm-thick devices under different surface finishes—critical point drying, chlorine plasma, hydrogen plasma, and oxygen plasma—measured at room temperature (RT) and 5K for both optical grade and electronic grade diamond. These two grades of diamond represent the ultimate loss limit (electronic grade) and the far better accessibility (optical grade). Using X-ray photoelectron spectroscopy (XPS) spectra (SI Fig. A.1), we found that oxygen plasma treatment offers the optimal balance between plasma-induced damage and surface passivation, achieving the highest  $Q_{\text{int}}$  overall. (f) Temperature-dependent measurements of two typical soft-clamped devices (100 nm thick, lightly tensioned at 30 MPa) from two co-processed electronic grade and optical grade diamond plates. Albeit differing resonant frequencies (o-grade: 200 kHz, e-grade: 154 kHz) and temperature dependence, both traces match well with the Arrhenius thermal relaxation model featuring an activation energy of  $\hbar\Delta = 0.035$  eV and tunneling rate of  $\Delta_0 = 9.1$  MHz, suggesting one shared type of thermally activated two-level systems associated with graphitized surfaces. Another family of defects limits the quality factor below 50 K, with electronic-grade diamond performing approximately twice as well as optical-grade. Inset shows the averaged  $Q_{\text{int}}$  at 5 K after correction for dissipation dilution, highlighting different thickness ( $h$ ) dependences: electronic-grade diamond is primarily surface-loss limited ( $Q_e = 1.6 \times 10^6 \times h/100 \text{ nm}$ ), whereas optical-grade diamond is additionally limited by bulk losses ( $Q_o^{-1} = (0.83 \times 10^6 \times h/100 \text{ nm})^{-1} + (1.6 \times 10^6)^{-1}$ ), likely due to nitrogen impurity-related defect dynamics.

tion is transformed into an enabling tool for dissipation dilution in diamond and potentially many other crystalline materials. This approach enables mechanical quality factors substantially enhanced by dissipation dilution, surpassing state-of-the-art devices of similar aspect ratios (comparison see Fig. 1(a)) by a significant margin, using NV-rich optical-grade diamond typically optimized for quantum applications over mechanical quality. Our demonstration significantly advances strain-engineering of cryogenic crystalline resonators towards mechanical quality factors previously predicted to exceed  $10^{13}$ , paving the way toward ultra-sensitive force detection, exploration of macroscopic quantum phenom-

ena, and realization of hybrid spin-mechanical quantum technologies.

## I. MATERIAL LOSSES OF HIGH-ASPECT-RATIO DIAMOND NANOMECHANICS

Diamond is an ideal candidate for ultracoherent nanomechanics due to its exceptionally low intrinsic acoustic damping at cryogenic temperatures. Unlike silicon, diamond surfaces are inert with no native oxide layer, leading to significantly lower nanoscale mechanical

losses [17]. However, nanomechanical structures in diamond are sensitive to second-order effects—including bulk impurities, subsurface damages, and surface chemistry—which become prominent only in near-ideal crystal materials and must be carefully controlled to realize the full potential of the platform.

We start by investigating and engineering the diamond loss mechanics at the nanoscale in order to achieve optimal intrinsic quality factors. Our devices are made using quasi-isotropic etching that results in single-crystal diamond nanostructures capable of supporting extremely high-aspect-ratio geometries approaching millimeter in length. This approach allows versatile control over device thickness and surface properties, essential for the application of strain engineering techniques. Optical and SEM images of these nanobeam structures, along with a simplified fabrication flow, are illustrated in Fig. 2(a-d). Utilizing this technique, we successfully suspend 100-nm thin diamond nanostrings approaching lengths of 2 mm within trenches of only  $5\text{ }\mu\text{m}$  deep, among the highest aspect ratios demonstrated in diamond nanomechanics. Note that deep trenches are important to avoid surface stiction.

To systematically identify optimal conditions for minimizing diamond losses, we characterized intrinsic mechanical quality factors across different CVD diamond grades—optical-grade (o-grade,  $\sim 200\text{--}300$  ppb nitrogen impurities) and electronic-grade (e-grade, impurities below 1 ppb)—subjected to various surface finishing methods, including critical point drying, chlorine plasma, hydrogen plasma, and oxygen-based treatments (plasma and wet chemical oxidation). The electronic-grade diamond sets the benchmark for acoustic performance, whereas the optical-grade provides a more accessible alternative albeit with higher impurity concentrations. The resulting mechanical quality factors of non-tensioned 100-nm-thick devices are presented in Fig. 2(e) (XPS surface chemical analysis in Supplementary Information (SI) section A). The oxygen termination consistently delivered the highest mechanical quality factors, balancing minimal surface damage (graphitization) and effective passivation (hydrophilic), while chlorine plasma significantly degraded device performance due to doping-induced lattice expansion.

We then used hierarchical soft-clamped designs [23] ( $\alpha \rightarrow 0$ , see Fig. 2(b)) to mitigate radiation losses at the clamping boundary, enabling direct access to intrinsic material losses (gas damping analysis see SI Fig. B.1). Temperature-dependent measurements (see Fig. 2(f)) reveal a common loss mechanism in both diamond grades, matching well with an Arrhenius thermal relaxation model [24] featuring an activation energy of  $0.035\text{ eV}$  and tunneling rate of  $9.1\text{ MHz}$ , indicative of thermally activated two-level systems likely associated with surface graphitization [25]. At temperatures below  $50\text{ K}$ , a distinct loss mechanism emerges (discussion see SI Section B), with electronic-grade diamond outperforming optical-grade by approximately two-fold at  $5\text{ K}$ . Correct-

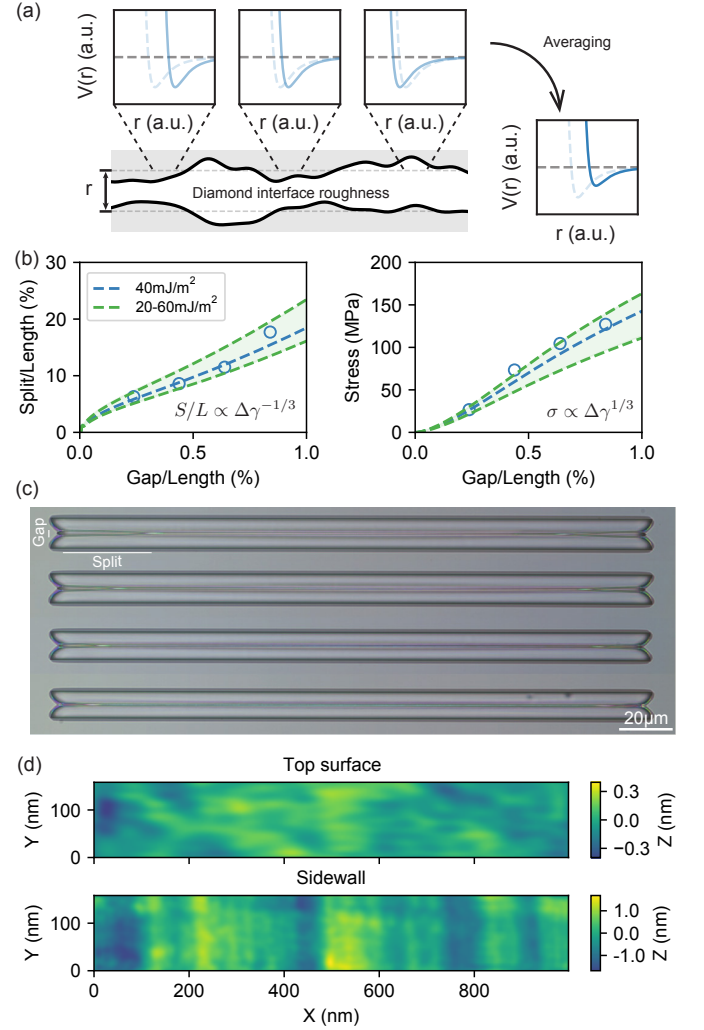


**FIG. 3. Characterizing van der Waals (vdW) adhesion energy.** (a) Illustration showing how rigid surface roughness ( $R$ ) reduces the effective vdW surface potential  $\Delta\gamma = f\Delta\gamma_{\text{ideal}}$ , compared to the ideal interface ( $\Delta\gamma_{\text{ideal}} = 83\text{ mJ/m}^2$ ). This effect is quantified by the Rabinovich-Rumpf factor  $f(R)$ , which averages the vdW interaction across varying nanoscale surface offsets. (b) Experimental characterization of vdW adhesion in individual double-beam devices with uniform width ( $171\text{ nm}$ ), correlating the length of the adhered region (or split length) to the beam separation gap (see optical image in (c)). Comparison with FEM simulations enables extraction of the effective vdW surface potential, yielding approximately  $40\text{ mJ/m}^2$  with variation corresponding to sidewall roughness between  $0.3\text{--}0.6\text{ nm}$  across devices. (d) Atomic force microscopy (AFM) surface topography maps of the top surface and sidewall of representative devices, with the sidewall roughness  $R = 0.5\text{ nm}$  consistent with the adhesion energy deduced from the split-gap analysis.

ing for dissipation dilution, we identify a linear surface-loss-limited trend for electronic-grade diamond ( $Q_{\text{surf}} \approx 1.6 \times 10^6 \times h/100\text{ nm}$ ), whereas optical-grade diamond exhibits additional bulk losses, likely arising from nitrogen impurities. Given its broader availability and reduced cost, optical-grade diamond is used exclusively in subse-



quent device studies.

## II. VAN DER WAALS SELF-ASSEMBLY OF STRAINED DIAMOND NANOMECHANICS

Given the exceptional intrinsic quality factors attainable in diamond, substantial enhancements are possible from dissipation dilution. Theoretical analysis (Fig. 1(a)) indicates that mechanical quality factors far exceeding current benchmarks are achievable through modest device dimensions ( $<500\ \mu\text{m}$  footprint,  $100\ \text{nm}$  thickness) under tensile strains significantly below diamond's elastic yield strain.

Next, we introduce an approach leveraging intrinsic van der Waals (vdW) surface interactions to engineer substantial tensile strains directly within monolithic diamond nanomechanical devices. Van der Waals forces are quantum-mechanical interactions originating from spontaneous polarization fluctuations of electron clouds on material surfaces, analogous to a short-range version of Casimir forces. For diamond—a particularly well-characterized material—this vdW adhesion energy can be precisely evaluated from first-principles calculations [26, 27], given by  $\Delta\gamma_{\text{diamond}} = 88\ \text{mJ/m}^2$ . However, since we observed graphitization on the surface from our fabrication process, we estimate a modified adhesion energy [28] to be  $\Delta\gamma_{\text{ideal}} \approx 80\ \text{mJ/m}^2$  (discussion in SI Section C).

In realistic devices, nanoscale surface roughness significantly reduces the effective vdW potential by spatial averaging of the originally sharp surface interaction profile (see Fig. 3(a)). This roughness effect is quantitatively described by the Rabinovich–Rumpf factor [29] (expression see SI Section C). To precisely determine the effective vdW adhesion achievable in our fabricated diamond nanostructures, we use a double-beam geometry (see illustration in Fig. 1(b) and optical images in Fig. 3(c)), where two uniform nanomechanical beams adhere upon contact due to vdW attraction, balancing with the decohesion forces at an angle. Experimentally measured beam adhesion lengths, compared with finite-element modeling (Fig. 3(b)), yield effective vdW surface energies of  $20\text{--}60\ \text{mJ/m}^2$ , first measurements of vdW adhesion energy for diamond surfaces, directly corresponding to sidewall roughness values of  $0.3\text{--}0.6\ \text{nm}$ —among the lowest reported in diamond nanofabrication [30]. Supporting this, destructive atomic force microscopy (AFM) measurements yield consistent roughness values around  $R = 0.5\ \text{nm}$  (Fig. 3(d)). Notably, the vdW-based method offers a universally applicable, non-destructive evaluation of nanoscale surface roughness, an essential tool for optimizing strain via adhesion, as the achievable tensile stress scales as  $\sigma \propto \Delta\gamma^{1/3}W^{-2/3}$ , where  $W$  is the beam width (see Fig. C.1).

Leveraging these insight, we optimized our device geometry by tapering down the clamping regions (simulation in Fig. 1(c) and scaled SEM image in Fig. 4(a))

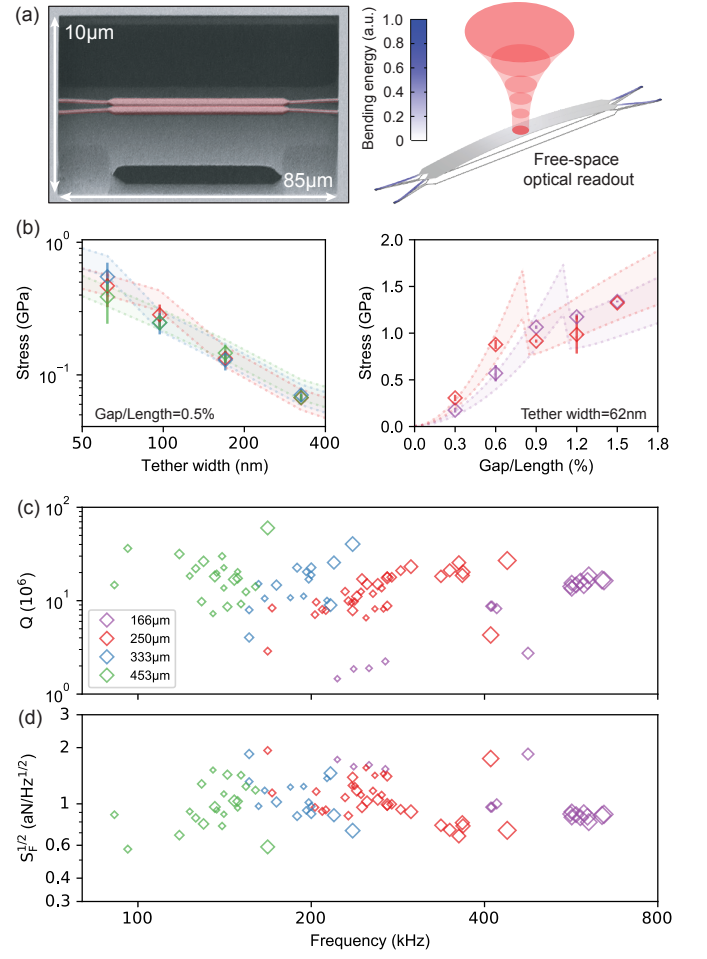


**FIG. 4. GPa-strain engineering through vdW self-assembly.** (a) False-color SEM image of clamp-tapered vdW self-assembled beams (vertical and horizontal axes scaled differently; image angle: 45 degrees). The wide regions enable efficient free-space optical readout as illustrated in the right panel, while the narrow regions reduce decohesion force, localizes tensile stress and bending energy density (deformation-induced dissipation) to enhance dissipation dilution. (b) Measured average tensile stresses of optical-grade devices in various lengths (color-coded) as a function of clamp widths and gaps, closely matching FEM predictions using vdW surface potentials between  $30\text{--}80\ \text{mJ/m}^2$ . Discontinuities in simulated curves correspond to decohesion events between contacting surfaces, verified by optical microscopy (see SI Fig. C.3). (c,d) Acoustic quality factors, force sensitivity and corresponding resonance frequencies are also summarized, showing enhancement from stress (encoded in marker size).

to reduce mechanical tearing forces, enabling controlled tensile stresses exceeding  $1\ \text{GPa}$ . The clamp-tapered design [31] also facilitates efficient free-space optical readout of mechanical displacement at the beam's center. To further enhance the yield of self-assembled devices, we employed picoliter-scale water condensation to achieve sidewall adhesion while mitigating unintended vdW adhesion to the substrate surface (details see Fig. C.2), re-

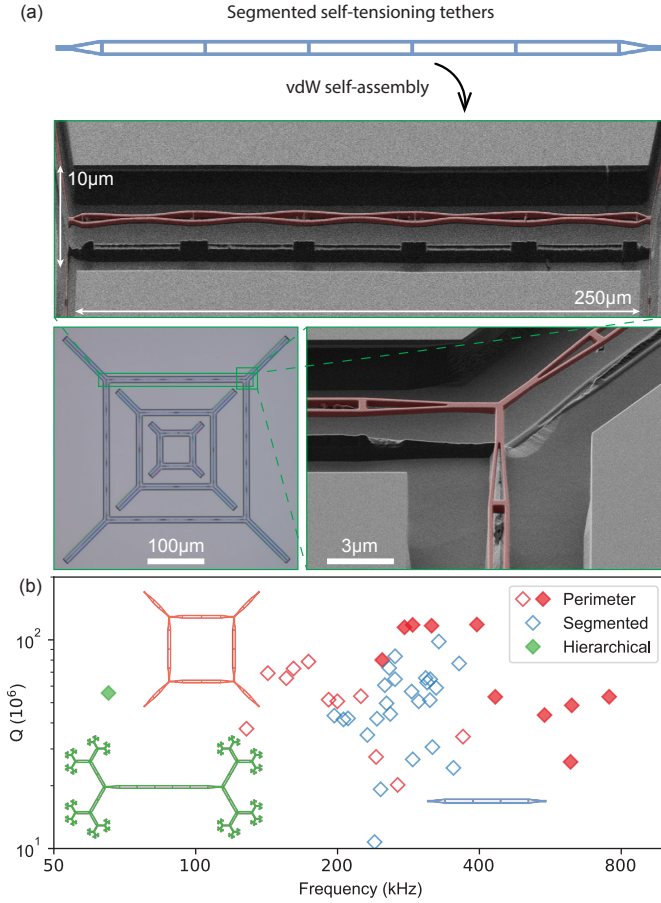


**FIG. 5. vdW self-assembly of complex nanomechanical networks for soft clamping.** (a) Schematic, optical, and scanning electron microscopy (SEM) images of a multi-tethered diamond perimeter-mode resonator assembled via van der Waals (vdW) adhesion, where self-tensioning segmented tethers induce significant tensile stress in the tether network. (b) Comparison of mechanical quality factors for the first few soft-clamped (solid) and hard-clamped (open) modes in perimeter-mode resonators (red, 250  $\mu\text{m}$  length), alongside the fundamental modes of hierarchical resonators (solid green, 830  $\mu\text{m}$  length) and segmented clamp-tapered resonators (open blue, 400  $\mu\text{m}$  length), all fabricated by vdW self-assembly. A substantial quality factor enhancement is observed in soft-clamped modes, achieving  $Q > 10^8$  at effective uniform stresses of only 200 MPa (Gap/Length up to 1%), relaxed by anisotropic etch-induced cross-sectional non-uniformities. More uniform tether orientations in clamp-tapered resonators enable clamp stresses exceeding 1 GPa (Gap/Length up to 1.5%), demonstrating significant dissipation dilution despite hard clamping.

sulting in a remarkable 93 % self-assembly success rate for devices up to 500  $\mu\text{m}$  in length, demonstrating compatibility with mass fabrication and extreme high-aspect-ratio structures.

As shown in Fig. 4(b), the measured maximum tensile stress reached 1.3 GPa, as evaluated from resonant frequency measurements. Across devices, our results are

well-described by vdW surface potentials ranging from 30-80  $\text{mJ}/\text{m}^2$ . Stress enhancement at narrower clamp widths arises from a combination of factors, including improved vdW adhesion due to reduced decohesion force and stress redistribution from the width modulation; the latter can contribute up to a twofold enhancement, factoring in thickness variations inherent in quasi-isotropic etching. Remarkably, we observed negligible added mechanical losses from the vdW adhesion interface itself, with intrinsic quality factors  $Q_{\text{int}} = 3 \times 10^5$  closely matching expectation from the effective increase in surface-volume ratio. This robustness is enabled by both the exceptional diamond interface quality and the symmetric geometry of the vdW adhesion plane, minimizing interfacial distortion under mechanical vibration.

Given sufficient tensile stress and high aspect ratio, further enhancement of mechanical coherence can be realized by adopting soft-clamped architectures, which exhibit a quadratic scaling of quality factor with device footprint—a significant advantage over the linear scaling observed in hard-clamped beam structures (Fig. 1(a)). To fully leverage this scaling, however, the vdW self-assembly method must be generalized to more complex string network geometries that underpin soft-clamping strategies.

Here, we demonstrate precisely this capability: Fig. 5 shows the successful implementation of vdW self-assembly to induce tensile strain in complex multi-tethered nanomechanical networks. By employing a segmented self-tensioning tether as an elementary building block, our method greatly simplifies the design process and enables straightforward extension of vdW self-assembly to arbitrary string-network geometries across diverse length scales. Using this approach, we fabricate diamond resonators supporting soft-clamped modes and observe clear quality factor enhancements relative to hard-clamped modes at comparable frequencies, consistent with improvements achieved through soft clamping [23]. Remarkably, even at ultra-compact device dimensions, we achieve mechanical quality factors exceeding 100 million at liquid-helium temperatures, representing substantial improvement over state-of-the-art resonators of comparable dimensions [9]. These results firmly establish vdW-assisted dissipation dilution as a powerful pathway for ultracoherent nanomechanical systems.

### III. CONCLUSIONS

We have demonstrated a novel strain-engineering approach for diamond nanomechanical systems, that leverages van der Waals (vdW) self-assembly to achieve tensile stresses beyond 1 GPa while preserving the intrinsic material properties. When applied to soft-clamped resonator designs, this approach enables mechanical quality factors exceeding 100 million, representing the highest values reported to date for strained nanomechanical

ics at this scale, despite operating under lower tensile strain and fabricated on readily available optical-grade diamond (roughly an order of magnitude less expensive than electronic-grade diamond). Our vdW-engineered diamond nanobeams also feature excellent force sensitivity, estimated to be  $S_F^{1/2} = 0.5 \text{ aN/Hz}^{1/2}$  (Fig. 4(d)) at liquid-helium temperature, which is among the best performance for nanomechanical devices [32], and reaches that of the best spin-functional devices at mK temperature [17] where magnetic forces from single spins are measurable [33].

Beyond diamond, our vdW strain-engineering method is applicable to a broad class of material systems [10, 22, 34] that lack built-in stress, offering a general framework for implementing strain in quantum materials and devices. Softer single-crystal materials such as silicon and GaAs with similar surface potential can even achieve larger tensile strain for dissipation dilution. The GPa-level strain demonstrated here is also sufficient to alter the electronic structure of strain-sensitive defects, such as silicon-vacancy (SiV) centers [35], enabling their operation above 4 K by enhancing ground state splitting [36].

Moreover, the double-beam platform developed in this work provides a direct and non-destructive method to evaluate nanoscale surface roughness through the effective vdW surface potential—an essential metrology tool for photonic and mechanical systems where surface quality is critical [37]. Finally, the high-frequency breathing modes of our design generate relative motion between the vdW interfaces, offering a unique testbed for probing dynamical low-energy vdW physics [38]. This capability also enables direct characterization of electrical surface loss angles [39], providing insight into the fundamental limits of dissipation in nanostructured solids.

These results lay out a roadmap for achieving long-anticipated advancement in mechanical quality factors (theoretical prediction in Fig. 1(a)) using cryogenic crystalline resonators with soft-clamped designs. By enabling dissipation dilution with vdW self-assembly, our approach opens entirely new regimes for precision measurement (detailed discussion see SI Section D), including the detection of ultralight dark matter [40], tests of quantum gravity [41], and development of hybrid spin-mechanical interfaces for quantum information processing [42, 43], all made possible by transforming a longstanding fabrication nuance into a powerful tool for nanoscale science.

## ACKNOWLEDGMENTS

We thank Tobias Elbs for contributing to the early-stage experiment. We thank Rodrick K. Defo, Sukhad D. Joshi, Nils J. Engelsen, Chaoshen Zhang, Yiqi Wang for helpful discussions. This work was supported by AFOSR (Grant No. FA9550-23-1-0333), AWS (Grant No. A50791), and G.H. gratefully acknowledges financial support from the Swiss National Science Foundation (Postdoc.Mobility, grant number 222257), and Har-

vard’s Aramont Fellowship for Emerging Science Research. This work was performed in part at the Harvard University Center for Nanoscale Systems (CNS); a member of the National Nanotechnology Coordinated Infrastructure Network (NNCI), which is supported by the National Science Foundation under NSF award no. ECCS-2025158.

## CONTRIBUTIONS

G.H. conceived the idea for the project. G.H. performed the theoretical modeling, device design and analyzed the data. G.H., S.W.D. fabricated the devices. G.H., C.J. and S.W.D contributed to experimental setup and sample measurement. M.L., G.H supervised the project. All authors contributed to the writing of the manuscript.

## Supplementary Information

### Section A: Device fabrication and optimization

Suspension methods previously explored for diamond nanostructures include focused-ion beam milling [44], thin-film transfer methods [21, 44], angled etching [45], and quasi-isotropic etching [46]. Among these, quasi-isotropic etching uniquely provides precise three-dimensional control over device geometry—including slab thickness through adjustments in beam and trench widths—critical for nanoscale strain engineering.

We fabricate our devices from single-crystal diamond substrates sourced from Element Six in two grades: electronic-grade (nitrogen impurity <1 ppb, dislocation density  $\sim 10^4 \text{ cm}^{-2}$ ), representing the purest available diamond ideal for assessing fundamental loss limits; and more readily available optical-grade (nitrogen impurity 200-300 ppb), providing a lower bound on optimal mechanical performance.

The fabrication begins by coating the diamond substrates with a 200-nm PECVD silicon nitride (SiN) used as a hard mask in future steps, followed by spin-coating with 340 nm ZEP-520A resist. A thin conductive layer (5-nm gold) is deposited via electron-beam evaporation to reduce charging during electron-beam lithography. After lithographic exposure, the gold layer is chemically removed, and the ZEP resist is developed using N50 developer. The pattern is subsequently transferred into the SiN hard mask via reactive ion etching (RIE) using a  $\text{CF}_4/\text{C}_4\text{F}_8$  gas mixture. ZEP residues are then stripped by overnight immersion in PG remover at 80°C. Oxygen plasma vertical RIE is used to etch the pattern 800 nm deep into the diamond substrate.

To preserve sidewall smoothness during the critical isotropic undercut step, a conformal 40-nm alumina coating is applied using atomic layer deposition (ALD). A brief argon-chlorine RIE step selectively removes the top

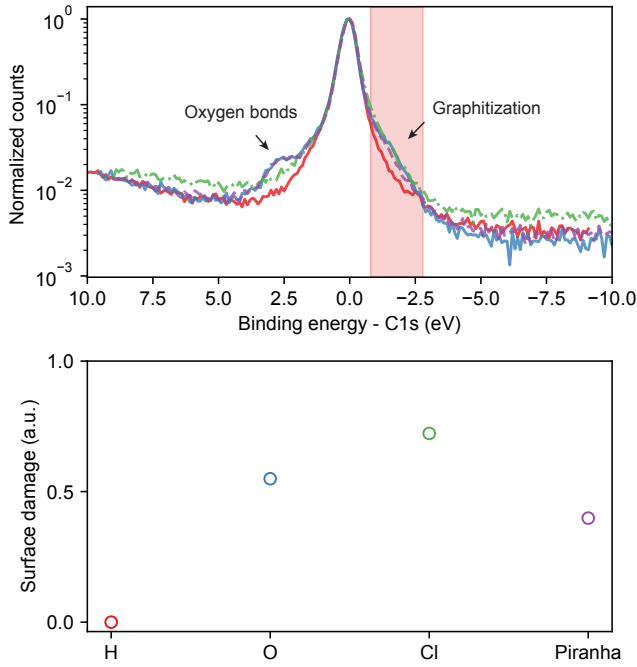


FIG. A.1. X-ray photoelectron spectroscopy (XPS) spectra (color-coded) of different surface treatment, centered on the carbon C1s peak, highlighting characteristic C-O bonding (2 eV) and plasma-induced graphitic (sp<sup>2</sup> carbon) damage (-1 eV, red shaded area). The integrated area of the sp<sup>2</sup> carbon component, normalized to the hydrogen termination, is shown in the lower panel. Oxygen plasma treatment offers the optimal balance between plasma-induced damage and surface passivation, achieving the highest  $Q_{\text{int}}$  overall. No significant change in  $Q_{\text{int}}$  was observed before and after piranha cleaning except partial recovery from plasma damage.

alumina layer, exposing the diamond surface for subsequent undercutting. High-power isotropic oxygen plasma etching then undercuts and releases the diamond devices, resulting in a controlled 5- $\mu\text{m}$  trench beneath each structure, which prevents unintended adhesion to the trench floor. Device thicknesses and uniformity are verified via scanning electron microscopy (SEM). The alumina protection ensures exceptionally smooth sidewalls necessary for consistent and reproducible van der Waals (vdW) adhesion.

Post-undercut cleaning involves a 2-min hydrofluoric acid (HF) etch followed by a 3-min hot Piranha solution treatment to remove residual contamination. Devices then undergo a final surface-finishing step, categorized as either wet or dry. The wet finish typically employs aqueous chemical treatments followed by an IPA rinse and blow-drying, while the dry finish involves critical-point drying (CPD), followed by brief oxygen plasma cleaning to remove CPD contaminants, and subsequent plasma-induced surface termination.

Surface finishing methods were systematically characterized using X-ray photoelectron spectroscopy (XPS) to correlate surface chemistry with mechanical quality fac-

TABLE I. Comparison of intrinsic acoustic quality factors  $Q_{\text{int}}$  for various high-aspect-ratio nanomechanical material platforms, highlighting differences between amorphous and crystalline phases and their respective thicknesses.

Material	Phase	$Q_{\text{int}}$	Thickness (nm)
SiN [9]	Amorphous	2.5e3	20
4K-Si [8]	Crystalline	8.0e3	14
InGaP [13]	Crystalline	8.1e3	73
AlN [14]	Crystalline	8.0e3	290
SiC [12]	3-C	1.2e3	100
SiCOI [11]	4-H	1.5e4	100
SiC [10]	4-H	2.8e4	100
SiC [48]	Amorphous	5.2e3	100
<b>4K-Diamond</b>	<b>Crystalline</b>	<b>1.3e6 (e-grade)</b> <b>5.4e5 (o-grade)</b>	<b>100</b>

tors (Fig.2(e), XPS data in Fig.A.1). We observed that CPD alone introduces significant contamination, resulting in the lowest quality factors. In contrast, oxygen-based finishes (via either plasma or wet oxidation treatments such as Piranha or tri-acid) yield optimal results for both diamond grades, with wet oxidation exhibiting marginally higher performance due to minimized surface graphitization. Oxygen termination provides hydrophilic passivation, creating an adsorbed water layer that protects against further surface contamination, as confirmed by XPS showing surface hydroxyl (-OH) groups.

While XPS data indicates hydrogen plasma effectively removes surface graphitization, however, hydrogen termination is hydrophobic and susceptible to contamination through polar gas adsorption, leading to conductive diamond surface, thus slightly reducing mechanical quality factors. Chlorine plasma treatment induces the most pronounced lattice damage, particularly severe in electronic-grade diamond. This damage manifests as significantly reduced mechanical quality factors and pronounced Duffing softening nonlinearities, indicating lattice expansion and doping by chlorine ions. The comparatively better resilience of optical-grade diamond under chlorine treatment suggests that higher impurity levels may mitigate chlorine-related doping by occupying available vacancy sites.

We observe that when the device thickness approaches 20 nm, significant expansion of the nanobeam occurs, causing it to collapse onto the substrate surface. This suggests the presence of an approximately 10 nm-thick graphitized surface layer resulting from high-energy plasma etching. Achieving stable thicknesses at the 10 nm scale will thus require gentler processing methods, such as atomic layer etching of diamond [47].



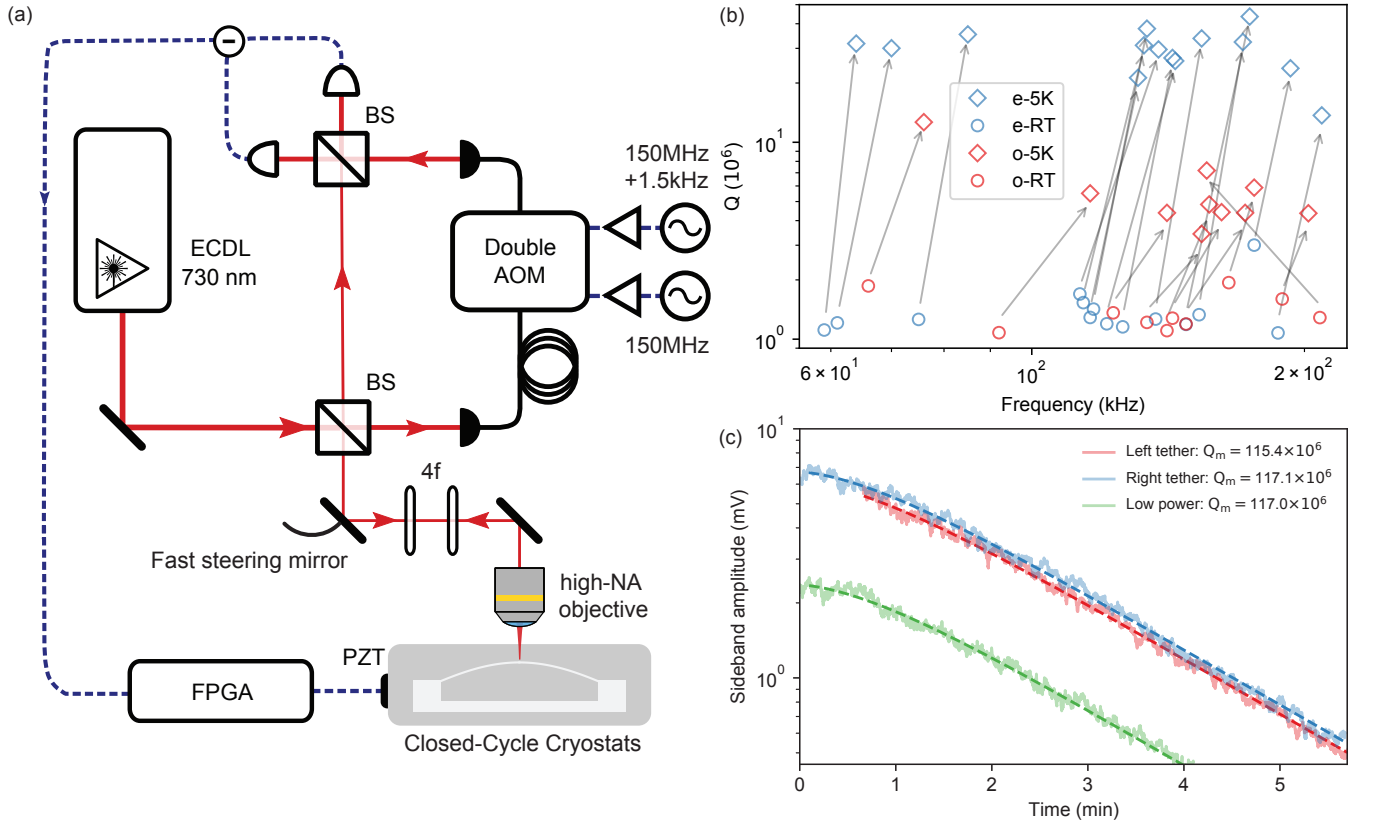


FIG. B.1. (a) Simplified scheme of the nanomechanics characterization setup. ECDL: external cavity diode laser, BS: beam splitter, AOM: acousto-optic modulator, PZT: piezoelectric actuator, FPGA: field-programmable gate array. (b) Comparison of mechanical quality factors for co-fabricated electronic-grade and optical-grade devices measured at room temperature (RT) and 5 K. All devices are 400-nm thick, under light tensile stress (25 MPa), and span lengths from 300  $\mu\text{m}$  to 2 mm. The observed quality factors exhibit minimal dependence, strongly indicating that gas damping is not the dominant loss mechanism. (b) Mechanical quality factors measured on a soft-clamped mode of a perimeter-mode resonator as a function of laser beam position and input power. The results show consistency within 2%, ruling out significant photothermal or optical backaction effects.

## Section B: Mechanical loss characterization

Mechanical quality factors of the diamond nanomechanical devices were characterized using a heterodyne Michelson interferometer setup (see Fig. B.1(a)). A 730 nm external-cavity diode laser (Toptica ECDL) provided approximately 1 mW optical power, from which less than  $10 \mu\text{W}$  was directed to the sample. The laser beam was focused onto the diamond resonator through a 4f-confocal optical system employing a high-NA (0.9) objective, yielding a 500-nm spot size comparable to the device width. Beam positioning was precisely controlled using a fast steering mirror. The reflected signal from the device was recombined with a local oscillator frequency-shifted by 1.5 kHz via a fiber-coupled double-acousto-optic modulator, enabling heterodyne detection with a balanced photodetector. This method effectively suppressed the need for active optical path-length stabilization during measurements.

Samples were affixed to a holder using fast-drying silver paste, and a miniature piezoelectric actuator (piezo)

to the backside of the holder using epoxy. This piezo actuator allowed acceleration-based excitation of mechanical resonances. The sample holder was integrated into an attodry cryostat capable of stable temperature sweeps from 5 K to 295 K, with measured external vacuum levels between  $2 \times 10^{-5}$  mbar and  $1 \times 10^{-6}$  mbar. Actual pressure at the sample stage was expected to be significantly lower during cryogenic operation.

Mechanical resonances were excited by sweeping the frequency of the piezo drive across resonance, while the resulting device displacement was tracked in real-time using a phase-locked loop (PLL). Resonance ring-down data obtained from the PLL provided both amplitude and frequency time-series, from which mechanical quality factors were directly extracted. Laser power was systematically varied to verify that measured quality factors were unaffected by photothermal amplification or damping (example see Fig. B.1(c)).

Due to the exceptionally high intrinsic quality factors achievable in diamond, identifying and isolating extrinsic loss channels is critical. Thermoelastic [49] and

Akhiezer [50] damping mechanisms were calculated to be negligible ( $Q > 10^8$ ) due to the high-aspect-ratio geometry, leaving gas damping and radiation losses at the device clamps as potential external loss sources. To robustly isolate intrinsic material losses, we utilized fractal soft-clamped resonators, designed specifically to exponentially suppress radiation losses at the clamping regions by over two orders of magnitude compared to conventional string geometries of comparable dimensions. Both electronic-grade and optical-grade diamond resonators underwent identical wet oxygen surface termination treatments prior to mechanical characterization.

Temperature-dependent quality factor measurements revealed similar overall loss behaviors across both diamond grades. At room temperature, devices exhibited a consistent upper-bound quality factor of approximately  $10^6$ , independent of resonance frequency (Fig. B.1(b)). This frequency independence effectively rules out gas damping [51] as the dominant loss mechanism, given that gas damping would scale as:  $Q_{\text{gas}} = 8.6 \times 10^8 \cdot (f_m/1[\text{MHz}]) \cdot (h/20[\text{nm}]) / (P/10^{-6}[\text{mbar}])$ .

Upon cooling below approximately 270 K, this loss channel was eliminated, revealing a loss mechanism associated with thermally activated defects [24] until 50 K associated with surface graphitization, as indicated by X-ray photoelectron spectroscopy (XPS, Fig. A.1). The measured activation energy (0.035 eV) and tunneling rate (9.1 MHz) of these defects are similar to previously reported loss processes observed in amorphous dielectric systems [25]. The difference in defect-related losses observed between optical-grade and electronic-grade diamond likely arises from nitrogen-impurity-enhanced loss dynamics, given nitrogen impurities constitute the primary compositional difference between these two diamond grades.

Below approximately 50 K, a distinct additional loss mechanism emerged. At these low temperatures, electronic-grade diamond consistently demonstrated approximately twice the quality factor of optical-grade diamond. Detailed analysis (Fig. 2(f)) indicates that this additional loss mechanism at cryogenic temperatures originates predominantly from surface defects introduced during oxygen plasma etching, consistent with previous findings [17] of surface-related TLS losses characterized by activation energies on the order of 13 GHz and exhibiting a temperature scaling of  $Q \sim T^{-1.6}$ . These insights confirm surface treatment as a critical step in optimizing low-temperature mechanical coherence in diamond nanostructures. The fitted average intrinsic mechanical quality factor of both electronic and optical grades at 4 K are compared to other material platforms in Table. I.

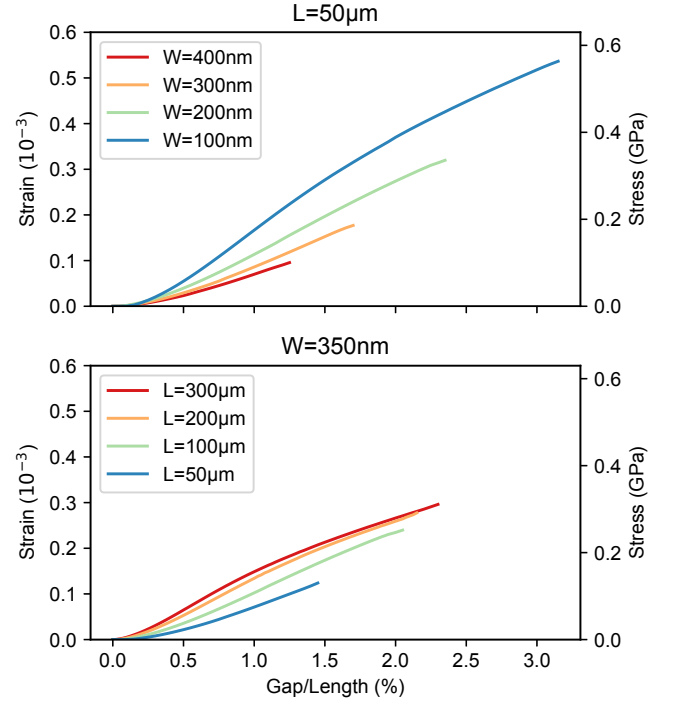


FIG. C.1. COMSOL simulation of vdW adhesion-induced tensile strain between pairs of uniform diamond beams, assuming an adhesion energy of  $\Delta\gamma = 80 \text{ mJ/m}^2$ . Beam width ( $W$ ) is varied at fixed length ( $L = 50 \mu\text{m}$ ), and the beam length is varied at fixed width ( $W = 350 \text{ nm}$ ). Resulting tensile strain is plotted against initial separation gap, with curves terminating at complete decohesion of the two beams.

### Section C: Van der Waals self-assembly

For diamond, first-principles calculations provide a reliable estimate of the ideal vdW surface adhesion energy:

$$\Delta\gamma_{\text{ideal}} = A_H / 12\pi z_0^2 \approx 80 \text{ mJ/m}^2$$

where  $A_H = 2.9 \times 10^{-19} \text{ J}$  is the Hamaker constant determined by Lifshitz theory [27], and  $z_0 = 0.3 \text{ nm}$  is the equilibrium vdW separation [26, 27]. This level of surface energy is modest due to the non-polar nature of diamond lattice. Due to surface graphitization observed from X-ray photoelectron spectroscopy (XPS) after oxygen plasma etching, we estimate a modest adjustment of the Hamaker constant to approximately  $A_H = 2.6 \times 10^{-19} \text{ J}$  (amorphous graphite layer), introducing a 10% uncertainty in the actual surface adhesion potential.

Realistically, nanoscale surface roughness significantly reduces the effective vdW adhesion potential through spatial averaging, described by the Rabinovich–Rumpf factor of a rigid body [29]:

$$f(R, \lambda) = \frac{8}{3} \left( \frac{z_0}{z_0 + R} \right)^2 \left( 1 + \frac{1}{(1 + 1.82 \frac{R}{z_0})^2} \right)$$

where  $R$  denotes surface roughness. Here, the expression is simplified in the large aperiodic length limit (60 nm

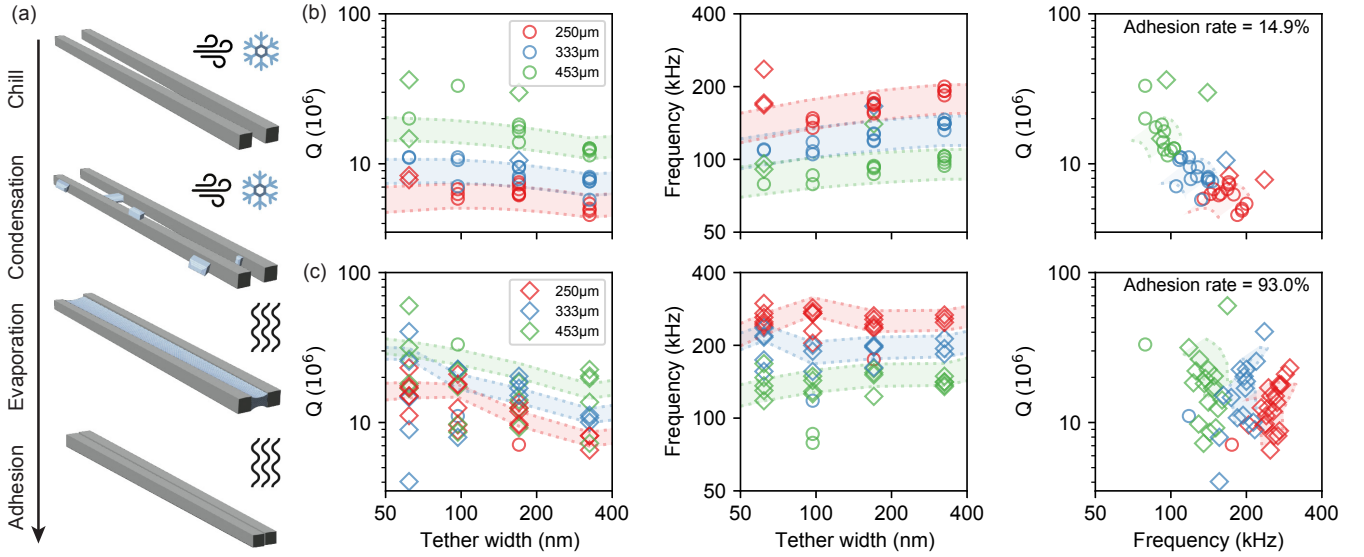


FIG. C.2. **(a)** Schematic of the liquid-assisted vdW self-assembly procedure. The devices are initially cryogenically cooled below the freezing point inside the cryostat and then briefly exposed to ambient air to induce controlled condensation to device surfaces. Condensation is halted by sealing the cryostat and initiating vacuum pumping. As the condensed water evaporates completely, devices self-assemble via vdW adhesion. **(b)** Mechanical quality factors and resonant frequencies measured at 5 K before self-assembly, plotted versus tether width. Devices unintentionally adhered after critical-point drying (15%) are indicated by diamond symbols, while non-adhered devices are represented by circles. **(c)** Post-self-assembly mechanical characterization at 5 K, showing a high self-assembly yield (93%). Shaded regions represent COMSOL simulation predictions for device frequency and mechanical quality factors, assuming surface adhesion energy between  $\Delta\gamma = 30 - 80 \text{ mJ/m}^2$  and the intrinsic mechanical quality factor  $Q_{\text{int}} = 3 \times 10^5$ . The discontinuity observed in simulation results corresponds to the decohesion phenomenon detailed in Fig. C.3. Notably, the device achieving the highest quality factor  $60 \times 10^6$  at  $453 \mu\text{m}$  fully adheres beyond simulation expectations, surpassing predicted partial decohesion behavior for this device length.

measured from AFM). The model assumes the interface is made up of a few widely spaced asperity summits rising from an otherwise flat valley floor, so adhesion is governed mainly by contacts between those summits and the opposing flat areas—an assumption that agrees well with the summit-valley pattern observed in our AFM measurements. To accurately quantify the effective adhesion potential of our fabricated devices, we employed a double-beam geometry, with two adjacent nanomechanical beams initially separated by a controlled gap (Fig. 3). Upon self-assembly through vdW adhesion, the adhered length depends on a competition between adhesion and mechanical tearing forces originating from the device clamps. Comparing experimentally measured adhesion lengths against finite-element (FEM) simulations allowed us to precisely extract the effective vdW potential on a device-by-device basis. This approach provides a universal, non-destructive method for evaluating side-wall roughness at the nanoscale, independent of device thickness.

Improving surface smoothness enables approaching the ideal adhesion potential and thus maximizing tensile stress, which scales approximately as  $\sigma \propto \Delta\gamma^{1/3}$ . From numerical simulation shown in Fig. C.1, the tensile stress favors narrow beam width ( $\sigma \propto W^{-2/3}$ ) and high aspect ratio. Narrow beam widths significantly enhance achievable stresses by effectively reducing the mechanical tear-

ing force. We therefore introduced tapered clamp regions, narrowing down to approximately 50 nm at device ends to minimize mechanical tearing and enhance tensile strain, while maintaining wider central regions suitable for high-efficiency free-space optical displacement read-out.

Realizing robust self-assembly in high-aspect-ratio structures has previously been challenging, with earlier techniques primarily limited to relatively short devices [52] ( $< 50 \mu\text{m}$ ). To address this, we developed a selective liquid-assisted vdW self-assembly process based on picoliter-scale water condensation, shown in Fig. C.2. Unlike conventional liquid immersion methods that risk undesired substrate adhesion, our approach confines condensation exclusively to suspended beam interfaces, resulting in a highly reproducible (93%) self-assembly success rate for devices up to  $500 \mu\text{m}$  long, thus compatible with scalable mass fabrication.

Experimentally, tensile stresses as high as 1.3 GPa were realized, closely matching FEM predictions for effective vdW potentials between  $30\text{--}80 \text{ mJ/m}^2$  (Fig. 4(b)). For devices with systematically varied separation gaps, both measurements and simulations consistently showed abrupt stress changes corresponding to sudden decohesion of partially adhered regions. This behavior was further corroborated through direct optical microscope observations (Fig. C.3), visually confirming decohesion



FIG. C.3. Optical microscope images of vdW self-assembled clamp-tapered diamond beams at various initial separation gaps, highlighting different decohesion thresholds in the wider beam regions. For beam lengths of  $166\ \mu\text{m}$ , decohesion occurs at a gap-to-length ratio of 1.2%; for beams  $250\ \mu\text{m}$  long, this occurs at a gap-to-length ratio of 0.9%. These observations align closely with stress measurements presented in Fig. 4(b), where the decohesion events manifest as distinct jumps in achievable tensile strain.

events at predicted gap thresholds.

Remarkably, intrinsic mechanical quality factors  $Q_{\text{int}} = 3 \times 10^5$  measured in double-beam optical-grade diamond structures (100 nm thickness), corrected for dissipation dilution, closely matched expectations derived from independent surface-loss characterization (Fig. 2(f)), after considering the increased surface-volume ratio around 50%. The absence of significant additional mechanical losses due to the vdW adhesion interface can be understood by the high-quality diamond surfaces and the symmetric alignment of the adhesion plane, minimizing dynamic interface distortions during mechanical os-

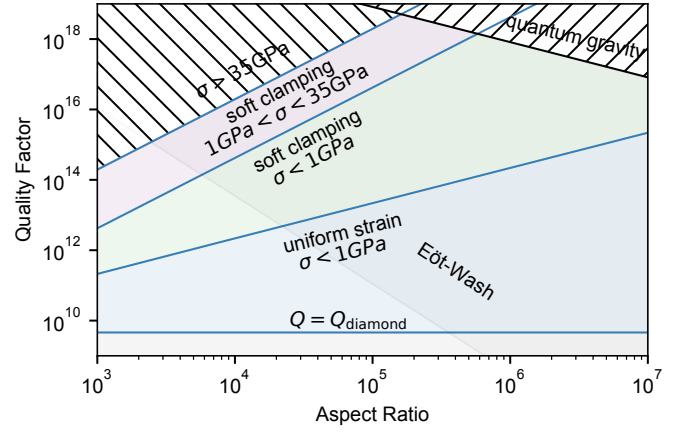


FIG. C.4. Estimate of quality factor of diamond nanomechanics accessible through dissipation dilution and mK-operation. Two parameter regimes are highlighted where low-energy physics can be probed using cryogenic mechanical oscillators. First is the current sensitivity bound set by the Eöt-Wash torsional balance experiment for the detection of ultra-light dark matter for one-day averaging using diamond nanomechanical systems. Second is the threshold where the non-classical nature of gravity can be examined through gravitationally induced transparency between two gravitationally interacting solid-state masses.

cillations. Our optimized vdW self-assembly therefore demonstrates both a practical solution for substantial tensile strain generation and a versatile methodology applicable broadly to other crystalline nanoscale platforms.

#### Section D: Projection of mK-operation

We estimate the optimal performance of strained single-crystal diamond nanomechanical oscillators operating at millikelvin (mK) temperatures. Prior studies [17] have reported that mechanical quality factors in diamond improve with decreasing temperature, following a scaling of  $Q \sim T^{-1.6}$ . Assuming this trend persists, and setting aside other factors such as radiation loss, gas damping, and emerging low-temperature loss channels, we project the achievable intrinsic quality factor at 1 mK, as shown in Fig. C.4.

Beyond reaching quality factors on par with optical clock transitions, these ultra-coherent oscillators are particularly promising for sensing weak forces in low-energy physics. Two notable applications include the detection of ultra-light dark matter and tests of the quantum nature of gravity—both of which demand extremely high acceleration sensitivity.

In the context of dark matter detection, one proposed method [53] involves a pair of mirrors composed of materials with different baryon-lepton (B-L) ratios. Due to coupling with a uniform background of hypothetical vector dark matter (“dark photons”), these mirrors experience a differential force, resulting in a measurable



relative displacement. The force can be optically read out, and the resulting data is used to place bounds on the coupling strength  $g$  of the dark matter. The current best bound is set by the Eöt-Wash torsion balance experiment at approximately  $g \approx 10^{-22}$ . For a resonant force sensor, the projected bound for  $g$  in the long-integration-time limit  $\tau \gg \tau_{\text{DM}}$  ( $\tau_{\text{DM}}$  the coherence time of the dark matter) is given by

$$g \sim \frac{1}{f_{12}a_0} \sqrt{\frac{4k_B T \Omega_{\text{DM}}^2}{m Q Q_{\text{DM}}} (\tau_{\text{DM}}/\tau)^{1/4}},$$

where  $a_0 = 3.7 \times 10^{11} \text{ m/s}^2$ ,  $Q_{\text{DM}} \sim 10^6$  is the effective quality factor of the dark matter, and  $f_{12} = 0.05$  accounts for the B–L ratio difference between the diamond and beryllium mirrors. The corresponding intrinsic quality factor required to beat the Eöt-Wash bound scales as  $Q_{\text{int}} \propto h/L^5$ , strongly favoring large aspect ratios. The required performance threshold by one-day integration is indicated by the light gray region in Fig. C.4.

Similarly, in the proposed scheme for testing the quantum nature of gravity via gravitationally induced transparency (GIT) [54], two mechanical resonators are brought into proximity such that their gravitational interaction dominates over the interaction with the environment bath (other forces eliminated by electrical shielding). For two semi-infinitely long string-like objects, the maximum gravitational coupling rate is given

by:

$$\lambda = Gm/Ld^2\Omega_m \approx \Omega_G^2/\Omega_m,$$

where  $G$  is the gravitational constant,  $m$  is the mass of the oscillator,  $L$  is the resonator length,  $d$  is the separation gap between the two,  $\Omega_m$  is the mechanical frequency, and  $\Omega_G = \sqrt{\pi G \rho} = 8.6 \times 10^{-4} \text{ Hz}$  is a gravitational material constant.

Since these are low frequency oscillators, it is useful to define environment bath frequency at unity phonon occupation  $\Omega_T = k_B T/\hbar$ . In the case where quantum signal can be transferred from one mechanical oscillator to the other, and the channel is not entanglement-breaking, then gravity must have a quantum nature (model independent). Mapping the system to a quantum thermal attenuator channel, the criteria for reaching this threshold is quantified as  $\Omega_G^2/\Gamma_m \Omega_T \geq 1$ , and equivalently the threshold for oscillator quality factor  $Q \geq \Omega_m \Omega_T/\Omega_G^2$ .

For soft-clamped resonators, the intrinsic quality factor needed to reach this regime scales as  $Q_{\text{int}} \propto h^2/L^3$ , again favoring high aspect ratios. This quantum gravity threshold is highlighted as the patched region in Fig. C.4.

We note that these projections are conservative. Cryogenic platforms based on nuclear demagnetization have demonstrated temperatures below  $100 \mu\text{K}$  [55], and further improvements—such as mass-loading in soft-clamped geometries—are expected to substantially lower the quality factor thresholds for both ultra-light dark matter detection and quantum gravity tests.

- 
- [1] R. Kubo, *Reports on Progress in Physics* **29**, 255 (1966).
  - [2] G. D. Cole, W. Zhang, M. J. Martin, J. Ye, and M. Aspelmeyer, *Nature Photonics* **7**, 644 (2013).
  - [3] G. D. Cole, S. W. Ballmer, G. Billingsley, S. B. Cataño-Lopez, M. Fejer, P. Fritschel, A. M. Gretarsson, G. M. Harry, D. Kedar, T. Legero, C. Makarem, S. D. Penn, D. H. Reitze, J. Steinlechner, U. Sterr, S. Tanioka, G.-W. Truong, J. Ye, and J. Yu, *Applied Physics Letters* **122**, 110502 (2023).
  - [4] M. Aspelmeyer, T. J. Kippenberg, and F. Marquardt, *Rev. Mod. Phys.* **86**, 1391 (2014).
  - [5] M. Imboden and P. Mohanty, *Physics Reports* **534**, 89 (2014), dissipation in nano-electromechanical systems.
  - [6] S. A. Fedorov, N. J. Engelsen, A. H. Ghadimi, M. J. Bereyhi, R. Schilling, D. J. Wilson, and T. J. Kippenberg, *Phys. Rev. B* **99**, 054107 (2019).
  - [7] D. J. Wilson, C. A. Regal, S. B. Papp, and H. J. Kimble, *Phys. Rev. Lett.* **103**, 207204 (2009).
  - [8] A. Beccari, D. A. Visani, S. A. Fedorov, M. J. Bereyhi, V. Boureau, N. J. Engelsen, and T. J. Kippenberg, *Nature Physics* **18**, 436 (2022).
  - [9] N. J. Engelsen, A. Beccari, and T. J. Kippenberg, *Nature Nanotechnology* **19**, 725 (2024).
  - [10] A. Hochreiter, P. Bredol, F. David, B. Demiralp, H. B. Weber, and E. M. Weig, *Monolithic 4h-sic nanomechanical resonators with high intrinsic quality factors* (2025), [arXiv:2501.17960 \[cond-mat.mes-hall\]](https://arxiv.org/abs/2501.17960).
  - [11] L. Sementilli, D. M. Lukin, H. Lee, J. Yang, E. Romero, J. Vučković, and W. P. Bowen, *Nano Letters* **25**, 6069 (2025).
  - [12] E. Romero, V. M. Valenzuela, A. R. Kermany, L. Sementilli, F. Iacopi, and W. P. Bowen, *Phys. Rev. Appl.* **13**, 044007 (2020).
  - [13] S. K. Manjeshwar, A. Ciers, F. Hellman, J. Bläsing, A. Strittmatter, and W. Wieczorek, *Nano Letters* **23**, 5076 (2023).
  - [14] A. Ciers, A. Jung, J. Ciers, L. R. Nindito, H. Pfeifer, A. Dadgar, A. Strittmatter, and W. Wieczorek, *Advanced Materials* **36**, 2403155 (2024).
  - [15] L. G. Villanueva and S. Schmid, *Phys. Rev. Lett.* **113**, 227201 (2014).
  - [16] C. Chia, B. Machielse, B. Pingault, M. Chalupnik, G. Joe, E. Cornell, S. W. Ding, S. Bogdanović, K. Kuruma, A. H. Piracha, S. Maity, T. M. Babinec, S. Meesala, and M. Lončar, in *Diamond for Quantum Applications Part 2*, Semiconductors and Semimetals, Vol. 104, edited by C. E. Nebel, I. Aharonovich, N. Mizuochi, and M. Hatano (Elsevier, 2021) pp. 219–251.
  - [17] Y. Tao, J. M. Boss, B. A. Moores, and C. L. Degen, *Nature Communications* **5**, 3638 (2014).
  - [18] J. E. Field, *Reports on Progress in Physics* **75**, 126505 (2012).
  - [19] A. Banerjee, D. Bernoulli, H. Zhang, M.-F. Yuen, J. Liu, J. Dong, F. Ding, J. Lu, M. Dao, W. Zhang, Y. Lu, and

- S. Suresh, *Science* **360**, 300 (2018).
- [20] C. Dang, J.-P. Chou, B. Dai, C.-T. Chou, Y. Yang, R. Fan, W. Lin, F. Meng, A. Hu, J. Zhu, J. Han, A. M. Minor, J. Li, and Y. Lu, *Science* **371**, 76 (2021).
- [21] X. Guo, N. Deegan, J. C. Karsch, Z. Li, T. Liu, R. Shreiner, A. Butcher, D. D. Awschalom, F. J. Heremans, and A. A. High, *Nano Letters* **21**, 10392 (2021).
- [22] B. Machielse, S. Bogdanovic, S. Meesala, S. Gauthier, M. J. Burek, G. Joe, M. Chalupnik, Y. I. Sohn, J. Holzgrafe, R. E. Evans, C. Chia, H. Atikian, M. K. Bhaskar, D. D. Sukachev, L. Shao, S. Maity, M. D. Lukin, and M. Lončar, *Phys. Rev. X* **9**, 031022 (2019).
- [23] M. J. Bereyhi, A. Arabmoheghi, A. Beccari, S. A. Fedorov, G. Huang, T. J. Kippenberg, and N. J. Engelsen, *Phys. Rev. X* **12**, 021036 (2022).
- [24] G. Cannelli, R. Cantelli, M. Capizzi, C. Coluzza, F. Cordero, A. Frova, and A. Lo Presti, *Phys. Rev. B* **44**, 11486 (1991).
- [25] R. O. Pohl, X. Liu, and E. Thompson, *Rev. Mod. Phys.* **74**, 991 (2002).
- [26] W. Sun, Q. Zeng, and A. Yu, *Chemical Engineering Science* **121**, 23 (2015), 2013 Danckwerts Special Issue on Molecular Modelling in Chemical Engineering.
- [27] L. Bergström, *Advances in Colloid and Interface Science* **70**, 125 (1997).
- [28] P. Toliás, *Fusion Engineering and Design* **133**, 110 (2018).
- [29] Y. I. Rabinovich, J. J. Adler, A. Ata, R. K. Singh, and B. M. Moudgil, *Journal of Colloid and Interface Science* **232**, 10 (2000).
- [30] N. Quack, C. Galland, and E. Losero, in *Nanophotonics with Diamond and Silicon Carbide for Quantum Technologies*, Nanophotonics, edited by M. Agio and S. Castelletto (Elsevier, 2025) pp. 27–45.
- [31] M. J. Bereyhi, A. Beccari, S. A. Fedorov, A. H. Ghadimi, R. Schilling, D. J. Wilson, N. J. Engelsen, and T. J. Kippenberg, *Nano Letters* **19**, 2329 (2019).
- [32] A. Eichler, *Materials for Quantum Technology* **2**, 043001 (2022).
- [33] D. Rugar, R. Budakian, H. J. Mamin, and B. W. Chui, *Nature* **430**, 329 (2004).
- [34] P. K. Shandilya, J. E. Fröch, M. Mitchell, D. P. Lake, S. Kim, M. Toth, B. Behera, C. Healey, I. Aharonovich, and P. E. Barclay, *Nano Letters* **19**, 1343 (2019).
- [35] S. Meesala, Y.-I. Sohn, B. Pingault, L. Shao, H. A. Atikian, J. Holzgrafe, M. Gündoğan, C. Stavarakas, A. Sipahigil, C. Chia, R. Evans, M. J. Burek, M. Zhang, L. Wu, J. L. Pacheco, J. Abraham, E. Bielejec, M. D. Lukin, M. Atatüre, and M. Lončar, *Phys. Rev. B* **97**, 205444 (2018).
- [36] P.-J. Stas, Y. Q. Huan, B. Machielse, E. N. Knall, A. Suleymanzade, B. Pingault, M. Sutula, S. W. Ding, C. M. Knaut, D. R. Assumpcao, Y.-C. Wei, M. K. Bhaskar, R. Riedinger, D. D. Sukachev, H. Park, M. Lončar, D. S. Levonian, and M. D. Lukin, *Science* **378**, 557 (2022).
- [37] F. P. Payne and J. P. R. Lacey, *Optical and Quantum Electronics* **26**, 977 (1994).
- [38] A. I. Volokitin and B. N. J. Persson, *Rev. Mod. Phys.* **79**, 1291 (2007).
- [39] N. P. de Leon, K. M. Itoh, D. Kim, K. K. Mehta, T. E. Northup, H. Paik, B. S. Palmer, N. Samarth, S. Sangtawesin, and D. W. Steuerman, *Science* **372**, eabb2823 (2021).
- [40] G. Bertone and T. M. P. Tait, *Nature* **562**, 51 (2018).
- [41] C. Marletto and V. Vedral, *Phys. Rev. Lett.* **119**, 240402 (2017).
- [42] F. Fung, E. Rosenfeld, J. D. Schaefer, A. Kabcenell, J. Gieseler, T. X. Zhou, T. Madhavan, N. Aslam, A. Yacoby, and M. D. Lukin, *Phys. Rev. Lett.* **132**, 263602 (2024).
- [43] G. Joe, M. Haas, K. Kuruma, C. Jin, D. D. Kang, S. W. Ding, C. Chia, H. Warner, B. Pingault, B. Machielse, S. Meesala, and M. Loncar, *arxiv:2503.09946* (Submitted).
- [44] T. M. Babinec, J. T. Choy, K. J. M. Smith, M. Khan, and M. Lončar, *Journal of Vacuum Science & Technology B* **29**, 010601 (2011).
- [45] M. J. Burek, Y. Chu, M. S. Z. Liddy, P. Patel, J. Rochman, S. Meesala, W. Hong, Q. Quan, M. D. Lukin, and M. Lončar, *Nature Communications* **5**, 5718 (2014).
- [46] B. Khanaliloo, M. Mitchell, A. C. Hryciw, and P. E. Barclay, *Nano Letters* **15**, 5131 (2015).
- [47] K. J. Kanarik, S. Tan, and R. A. Gottscho, *The Journal of Physical Chemistry Letters* **9**, 4814 (2018).
- [48] M. Xu, D. Shin, P. M. Sberna, R. van der Kolk, A. Cupertino, M. A. Bessa, and R. A. Norte, *Advanced Materials* **36**, 2306513 (2024).
- [49] R. Lifshitz and M. L. Roukes, *Phys. Rev. B* **61**, 5600 (2000).
- [50] T. O. Woodruff and H. Ehrenreich, *Phys. Rev.* **123**, 1553 (1961).
- [51] M. J. Martin, B. H. Houston, J. W. Baldwin, and M. K. Zalalutdinov, *Journal of Microelectromechanical Systems* **17**, 503 (2008).
- [52] H. Ashiba, R. Kometani, S. Warisawa, and S. Ishihara, *Journal of Vacuum Science & Technology B* **29**, 06FE02 (2011).
- [53] J. Manley, M. D. Chowdhury, D. Grin, S. Singh, and D. J. Wilson, *Phys. Rev. Lett.* **126**, 061301 (2021).
- [54] A. Mari, S. Zippilli, and D. Vitali, *Can gravity mediate the transmission of quantum information?* (2025), *arXiv:2504.05998* [quant-ph].
- [55] J. Yan, J. Yao, V. Shvarts, R.-R. Du, and X. Lin, *Review of Scientific Instruments* **92**, 025120 (2021).